Taylor & Francis
Taylor & Francis Group

Check for updates

On mean flow universality of turbulent wall flows. I. High Reynolds number flow analysis

Stefan Heinz

Mathematics Department, University of Wyoming, Laramie, WY, USA

ABSTRACT

The universality and mathematical physical structure of wall-bounded turbulent flows is a topic of discussions over many decades. There is no agreement about questions like what is the physical mean flow structure, how universal is it, and how universal are theoretical concepts for local and global flow variations. These questions are addressed by using latest direct numerical simulation (DNS) data at moderate Reynolds numbers Re and experimental data up to extreme Re. The mean flow structure is explained by analytical models for three canonical wall-bounded turbulent flows (channel flow, pipe flow, and the zero-pressure gradient turbulent boundary layer). Thorough comparisons with DNS and experimental data provide support for the validity of models. Criteria for veritable physics derived from observations are suggested. It is shown that the models presented satisfy these criteria. A probabilistic interpretation of the mean flow structure shows that the physical constraints of equal entropies and equally likely mean velocity values in a region unaffected by boundary effects impose a universal log-law structure. The structure of wall-bounded turbulent flows is much more universal than previously expected. There is no discrepancy between local logarithmic velocity variations and global friction law and bulk velocity variations. Flow effects are limited to the minimum: the difference of having a bounded or unbounded domain, and the variation range of mean velocity values allowed by the geometry.

1. Introduction

The understanding of the mathematical physical mean flow structure of wall-bounded turbulent flows is an important and vibrant topic of classical fluid mechanics for almost a century [1–36]. In this regard, it is of primary interest to explain the structure and physical relevance of mean flow variations in inner and outer scalings, to understand the universality of mean flow variations in inner scaling and the flow dependence of velocity variations in outer scaling. More specific questions are the following ones:

CONTACT Stefan Heinz ✉ heinz@uwyo.edu ⊡ Mathematics Department, University of Wyoming, Laramie, WY 82071, USA

This article has been republished with minor changes. These changes do not impact the academic content of the article.

Supplemental data for this article can be accessed here. https://doi.org/10.1080/14685248.2019.1566736

(Q1) Structure: What is the physical mean flow structure of wall-bounded flows (does it involve logarithmic variations; is there a new unified law instead of a log-law or power law)?

(Q2) Universality: How universal is the mean flow of wall-bounded turbulent flows (how does the flow considered affect the mean flow; is the log-law flow-dependent)?

(Q3) Theory: Are different formulations of log-law theory consistent (how universal is the von Kármán constant κ depending on the flow and log-law formulation considered)?

These questions, which represent open current research questions [31–36], will be addressed here for a wide range of Reynolds numbers with respect to three canonical wall-bounded turbulent flows: channel flow, pipe flow, and the zero-pressure gradient turbulent boundary layer (TBL). For simplicity, the zero-pressure gradient TBL will be referred to below simply as TBL. The focus here is on incompressible flows, i.e. compressibility effects [37–43] are not considered.

It is of interest to note that clarification on these questions is beneficial due to several reasons. First, an analytical mean velocity model can represent corresponding direct numerical simulation (DNS) and experimental information in the most accurate, complete, and general way (see the further discussions in this paper). Second, it can contribute to a deeper theoretical understanding by clarifying questions about the existence of log-law variations of the mean velocity with constant coefficients and enabling conclusions about the structure of wall-bounded turbulent flows at (infinitely) high Reynolds numbers (see the discussions in reference [44]). Third, it can significantly support the further development of computational methods for turbulent flow simulations. This concerns, for example, the development and validation of large-eddy simulation (LES) [45–50] and hybrid dynamic LES methods [51–57], which are often seen to be without alternative if complex turbulent flows at high Reynolds numbers have to be analyzed with computational resources that do not allow the use of DNS (or resolved LES).

Compared to a huge variety of suggestions made before about how the mean streamwise velocity can be analytically described, see [30–36,58–63] and the references therein, there are two relevant features of the developments presented here. First, in contrast to curve-fitting, the approach is strictly focused on the identification of veritable physics: see the detailed discussion of this question in Section 3.3. Second, latest DNS data (channel flow DNS data of Lee and Moser [64,65]; pipe flow DNS data of Chin et al. [66]; TBL DNS data of Sillero et al. [67,68]) are used for the development of the most accurate velocity model, and latest experimental data (channel flow data of Schultz and Flack [69]; pipe flow data of Hultmark et al. [70,71]; TBL data of Vallikivi et al. [72]) are used to test the model performance up to extreme Reynolds numbers. It is worth noting that other DNS data are also involved in the model validation reported below: channel flow DNS data of Lozano-Durán and Jiménez [73,74]; pipe flow DNS data of Ahn et al. [75]; TBL DNS data of Schlatter and Örlü [76,77].

The paper is organised as follows. The difficulty of deriving analytical conclusions about mean velocity variations is illustrated in Section 2. The development of a new analytical velocity model and its validation are presented in Section 3. Sections 4 and 5 summarise answers obtained to the questions Q1–Q3 described above and overall conclusions, respectively.

2. The problem considered

To prepare the following developments, let us first make the problem considered more specific. After a brief summary of basic log-law formulations, recent DNS and experimental data are used to explain the problem related to finding convincing support for the log-law (or, more general, an analytical model for the mean streamwise velocity).

2.1. The log-law

The log-law of the wall is often considered as a land mark result of fluid dynamics. It can be derived on the basis of fairly general assumptions [14,78,79]. The mean streamline velocity U^+ is considered to be a function of the wall distance y and the friction Reynolds number Re_τ. Here, y is normalised by δ, which is the half-channel height, pipe radius, or 99% boundary layer thickness with respect to channel flow, pipe flow, and the TBL, respectively. Hence, we have $0 \leq y \leq 1$ for channel and pipe flow. The superscript $+$ refers to inner scaling, and we use $y^+ = Re_\tau y$ for the inner scaling wall distance. The friction Reynolds number is defined by $Re_\tau = u_\tau \delta / \nu$, where u_τ is the friction velocity and ν is the kinematic viscosity. For a sufficiently high Reynolds number it is assumed that $U^+ = f(y^+)$ if $y \ll 1$ and $U_\infty^+ - U^+ = g(y)$ if $y^+ \gg 1$. Here, U_∞^+ refers to the centreline/freestream maximum velocity U_∞^+. Then, there will be an overlap region (usual notation applied for differentiating various flow regions [2,14] is shown in Figure 1) where the two scalings have to match, so we require equal derivatives $y^+ \partial U^+ / \partial y^+ = y^+ f'(y^+) = -y g'(y)$. The latter result implies $y^+ f'(y^+) = -y g'(y) = \kappa^{-1}$ because y^+ and y are independent variables. Here, κ refers to the von Kármán constant. The integration of $y^+ f'(y^+) = \kappa^{-1}$ then implies the log-law
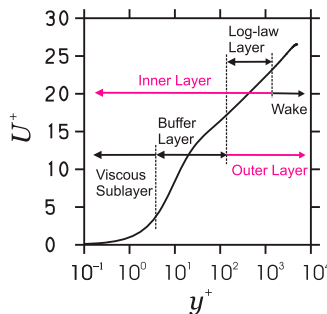
$$U^+ = \kappa^{-1} \ln y^+ + B. \tag{1}$$

B is a constant, and the integration of $-y g'(y) = \kappa^{-1}$ implies the velocity defect law,

$$U_\infty^+ - U^+ = -\kappa^{-1} \ln y + B_{def}, \tag{2}$$

where B_{def} refers to another constant. One consequence of the log-law is the friction law, which is obtained by combining the latter two expressions. It reads [2,27,80]

$$U_\infty^+ = \kappa^{-1} (\ln Re_\tau + C). \tag{3}$$

Figure 1. Channel flow DNS data of Lee and Moser [64,65] are shown for $Re_\tau = 5186$ in conjunction with layer notation used here.

The constant C is given by $C = \kappa(B_{def} + B)$. Another consequence of the log-law applies to the bulk velocity defined by $U_b^+ = \int_0^1 U^+ \, dy$. The integration of Equation (1) leads to

$$U_b^+ = \kappa^{-1}(\ln Re_\tau - 1) + B. \tag{4}$$

It is usual practice to consider a slightly extended version of Equation (1), which includes the wake region [4,81]. This equation, which is referred to by Pullin et al. [81,82] as the widely accepted log-wake law, reads

$$U^+ = \kappa^{-1} \ln y^+ + B + \Pi(y, Re_\tau). \tag{5}$$

Here, the function $\Pi(y, Re_\tau)$, which may depend on the flow considered, accounts for wake effects. Equation (5) is considered to be valid for $y_L^+/Re_\tau < y \leq 1$, where y_L^+ refers to a Reynolds number dependent lower limit of applicability of Equation (5).

2.2. Log-law validation by experiments and DNS

Let us consider the use of experimental data with respect to validating the log-law. Figure 2 shows pipe flow experimental data (including very high Re_τ cases) of the von Kármán constant κ with error bars, which are presented in Figure 5(a) of reference [27]. The κ values were obtained by using five data sets (the HVBS data are used in the study here: HVBS refers to data presented by Hultmark et al. [70,86]) and three equivalent consequences of the log-law: Equations (1), (3), and (4) were considered. In particular, the κ values were calculated by least-squares fits. With respect to Equation (1), e.g. U^+ was considered as a linear function of $\ln y^+$. It turns out that significantly different values of κ are obtained, depending on the specific log-law formulation considered. In addition, relatively large uncertainty intervals and discrepancies between results obtained from different data sets are reported [27]. Thus, this approach, which applies the highest Reynolds number data currently available, does not provide convincing support for the validity of the log-law. To overcome these issues, Bailey et al. [27] suggest to use improved instrumentation in order to obtain a more precise κ estimate.

As an alternative to the latter, let us try to use accurate DNS data at the highest Reynolds number available so far to address the validity of the log-law. To find an appropriate
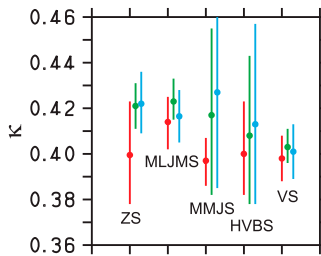
Figure 2. The von Kármán constant κ (dots) calculated from pipe flow experiments by using five data sets, see Figure 5(a) in reference [27]: ZS refers to Zagarola and Smits [83], MLJMS refers to McKeon et al. [84], MMJS refers to Morrison et al. [85], HVBS refers to Hultmark et al. [70,86], and VS refers to Vallikivi [87]. The error bars indicate the 95% confidence interval. The red values (on the left), green values (in the centre), and blue values (on the right) are based on least-squares fits to Equations (1), (3), and (4), respectively.
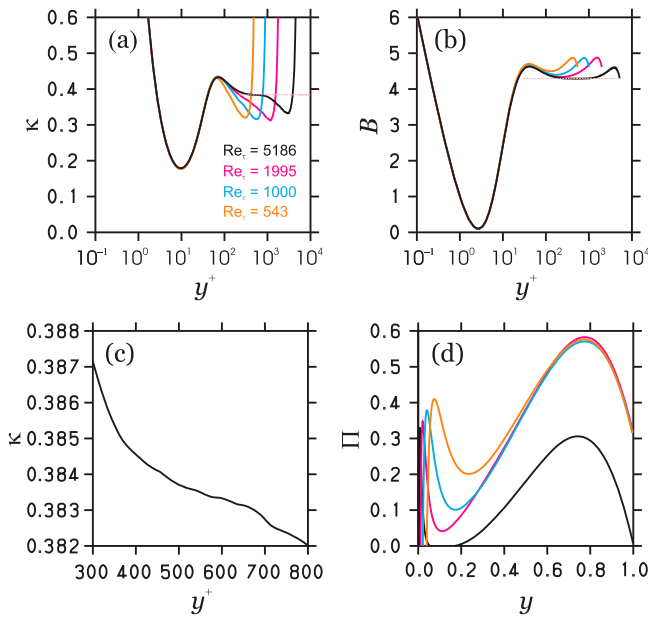
Figure 3. Figures (a), (b), (d) show $\kappa = 1/(S^+ y^+)$, $B = U^+ - \ln y^+/0.384$, and $\Pi = U^+ - \ln y^+/0.384 - 4.295$ according to Equations (1), (5), respectively, by using the channel flow DNS data of Lee and Moser [64,65]. The colour code used for different Re_τ is defined in (a). Figures (a) and (b) illustrate the constants $\kappa = 0.384$ and $B = 4.295$ by pink dashed lines, respectively. Figure (c) shows κ differently scaled for $Re_\tau = 5186$.

value for κ we consider Equation (1). Because B is constant, κ can be calculated by $\kappa = 1/(S^+ y^+)$, where $S^+ = \partial U^+/\partial y^+$ refers to the characteristic shear rate. The variation of κ is shown in Figure 3(a) for different Reynolds numbers by using the channel flow DNS data of Lee and Moser [64,65]. Here and in the following, no attempt is made to apply DNS data for $Re_\tau \leq 500$ because the use of the log-law is, basically, an inappropriate concept at such low Reynolds numbers. Only for the highest Reynolds number case $Re_\tau = 5186$ we see for $370 \leq y^+ \leq 670$ a plateau region where κ is approximately constant, $\kappa \approx 0.384$. In particular, we have $0.385 \geq \kappa \geq 0.383$ in this region. The use of Equation (1) combined with $\kappa = 0.384$ enables the calculation of $B = U^+ - \ln y^+/0.384$, which is shown in Figure 3(b). A constant B value is the requirement to calculate κ via $\kappa = 1/(S^+ y^+)$. For $Re_\tau = 5186$, it may be seen that there is indeed an extended region where we find a relatively constant B value, $B = 4.295$. In particular, we have $4.29 \leq B \leq 4.30$ for $240 \leq y^+ \leq 1050$.

However, the difficulties of this approach may be seen in Figure 3(c,d). With respect to $Re_\tau = 5186$, the variation of κ is shown in Figure 3(c) in the slightly extended plateau region of κ (see Figure 3(a)), this means for $300 \leq y^+ \leq 800$. This plot shows that $\kappa = 1/(S^+ y^+)$ is not strictly constant for the $Re_\tau = 5186$ case considered [88]. A discussion of the asymptotic variation of $1/(S^+ y^+)$ at extreme Re_τ can be found in reference [44]. According to Equation (5), Figure 3(d) shows the difference $\Pi = U^+ - \ln y^+/0.384 - 4.295$ between the DNS mean velocity and the log-law combined with constant κ and B. The Re_τ effect is not systematic: the maximum of Π for the highest $Re_\tau = 5186$ case

deviates for relatively large y significantly from the maxima of other Reynolds number cases.

Hence, current accurate DNS at a relatively high Reynolds number and experimental data at much higher Reynolds numbers cannot be used straightforwardly to provide evidence for the existence of a log-law that is characterised by a constant κ. The reason for that is the way to address this problem based on Equations (1), (3), and (4). Equation (1) can only be expected to be valid for sufficiently high Reynolds numbers (see reference [44]), i.e. the variation of the mean velocity in the log-layer is still overwhelmed by significant buffer layer and wake layer influences for the range of Re_τ considered [3]. Similarly, with respect to the use of Equations (3) and (4), the U_∞^+ data result from the superposition of different contributions to the mean velocity profile. In conclusion, the validation of the log-law requires the exclusion of (viscous sublayer/buffer layer and wake layer) contributions to the log-law in order to be able to separately study the log-law behaviour.

3. Model development and validation

As an alternative to existing developments, an analytical velocity model is introduced next. Section 3.1 describes the model and its validation versus DNS and experimental data up to high Re_τ (see also Appendices A and B). The accuracy of physics described in this way is addressed in Sections 3.2 and 3.3, and comparisons with other velocity models are presented in Section 3.4.

3.1. Model development

The model for the mean streamwise velocity U^+ described in Appendix A reads

$$U^+ = U_1^+ + \frac{1}{\kappa} \ln\left(\frac{1 + Hy^+/y_\kappa}{w + Ky}\right).$$ (6)

Here, the von Kármán constant $\kappa = 0.40$ (see the end of Appendix A.1 and second paragraph of Appendix A.2), $y_\kappa = 75.8$, U_1^+ is given by Equation (A.8), H is given by Equation (A.11), w is given by Equations (A.18), (A.19), and $K = y_\kappa^{-1} e^{\kappa U_{1\infty}^+ - C}$ is a flow-dependent constant given by $K = (0.933, 0.687, 0.285)$ for channel, pipe, and TBL flow, respectively. The mean velocity model given by Equation (6) will be referred to below as probabilistic velocity model (PVM) to reflect relevant features to be discussed in Section 4.1. The implied analytical model for the characteristic shear rate reads

$$S^+ = S_1^+ + S_2^+ + S_3^+ + S_1^{CP} + S_2^{CP}.$$ (7)

Here, S_1^+, S_2^+, S_3^+ are given by Equations (A.2), (A.12), (A.20), and S_1^{CP}, S_2^{CP} are given by Equations (S.3), (S.7): see the Supplementary Material. S_1^{CP} and S_2^{CP} are very small, but they matter regarding the calculation of turbulent viscosities (see reference [44]).

One key ingredient of the approach applied to derive the mean velocity model is the modal decomposition $U^+ = U_1^+ + U_2^+ + U_3^+$ of the velocity. Here, U_1^+ is given by Equation (A.8), $U_2^+ = \kappa^{-1} \ln(1 + Hy^+/y_\kappa)$, and $U_3^+ = -\kappa^{-1} \ln(w + Ky)$.

(1) The $U_1^+ = U_1^+(y^+)$ component reflects wall damping caused by the damping of vertical velocity fluctuations in the viscous sublayer. U_1^+ is constant ($= 15.85$) well away from the wall and damped towards the wall (see Figure A.1(a)).

(2) $U_2^+ = U_2^+(y^+)$ describes logarithmic velocity variations as predicted by log-law theory, but modified by H. H can be interpreted as transition probability for the onset of log-law variations. The appearance of such a transition probability is plausible: it provides the transition between two physically very different mechanisms (damping by the wall and logarithmic mean flow).

(3) $U_3^+ = U_3^+(y)$ describes variations in response to outer scaling. The term Ky determines the asymptotic wake contribution. Its linearity can be explained by the combination of U_2^+ and U_3^+, which shows that Ky balances asymptotically Hy^+/y_κ (which enables a constant U_∞^+). The contribution $0 \leq w \leq 1$ describes a transition probability (see the discussion of $F_w = 1 - w$ in Section 3.4). Its appearance is also plausible: it provides the transition between two physically very different mechanisms: logarithmic mean flow and the asymptotic wake stage.

Another key ingredient of the approach applied is the inclusion of governing equations and identification of linear physics regimes related to the modal velocity decomposition.

(1) The $U_1^+ = U_1^+(y^+)$ contribution to U^+ was obtained via the linear variation $ln(-\langle u'v'\rangle^+) \propto \ln y^+$ in conjunction with the momentum balance, see Appendix A.1. The transition function $0 \leq -\langle u'v'\rangle_1^+ \leq 1$ was justified by considering a corresponding linear relationship (see Figure A.1(c)).

(2) The $U_2^+(y^+) = \kappa^{-1}\ln(1 + Hy^+/y_\kappa)$ contribution to U^+ was obtained via the linear variation $U^+ \propto \ln y^+$, see Appendix A.1. The structure of the transition function $0 \leq H \leq 1$ was justified by considering a corresponding linear relationship (see Figure A.1(d)).

(3) The $U_3^+(y) = -\kappa^{-1}\ln(w + W_0)$ contribution to U^+ was determined in Appendix A.3. The asymptotic wake function W_0 was identified as linear function $W_0 = Ky$. The structure of the transition functions $0 \leq w \leq 1$ was justified by linear relationships presented in Figure A.4.

A comprehensive comparison of the velocity model given by Equation (6) versus both experimental data and DNS can be found in Appendix B. These comparisons are performed with respect to both moderate and high Re_τ. Overall, these comparisons with DNS and experiments reveal an impressive performance of the velocity model.

3.2. Observational physics criteria

After demonstrating that the velocity model obtained is in excellent agreement with DNS and experimental data, let us have a closer look at the accuracy of the velocity model obtained. It is known that the derivation of a complete analytical velocity model from the non-filtered Navier-Stokes equations is not possible for the flows (their boundary conditions) and Re_τ considered here [89]. Hence, the only possible way to address this problem is to use DNS and experimental data for the model design. The usual way to address such a problem is to use curve fitting. According to its general understanding, this means to find

an analytical curve that optimally reflects data without having clear evidence that the curve applied correctly agrees with the real physics. It is obvious that this approach, although it can be very beneficial, has a limited predictive power because of its lack of theoretical basis.

So there is the question of how it is possible to derive veritable physics for the case considered here. The following criteria for veritable physics derived from observations are suggested.

(C1)   A first criterion is that a model needs to represent a unique solution that is consistent with all relevant physics constraints (governing equations and boundary conditions).

(C2)   A second criterion should be proof that both modelled variables and their relevant derivatives accurately represent corresponding observations.

(C3)   A third criterion should be evidence according to (C2) for variations of model variables in response to all relevant scalings (inner and outer scalings for the case considered).

In particular, the second criterion (C2) is based on the general understanding of physics based conclusions to represent consequences of equations based on physical principles (combined with the fact that such equations usually relate derivatives of variables considered). The most convenient way to demonstrate this is to provide such evidence via scatterplots of observed versus predicted variables. Ideally, such plots result in 1:1 lines.

3.3. Observational physics validation

Does the velocity model presented here satisfy the criteria for veritable physics derived from observations described in the preceding paragraph? The first criterion is satisfied by the way in which this model was constructed. The question about whether or not the other two criteria are satisfied will be addressed in two steps. First (to focus in the following on velocity variations in response to inner scaling), the suitability of modelling velocity variations in response to outer scaling is considered. One way of doing this is to consider the deviation w from the asymptotic wake function $W_0 = Ky$, which is shown in Figure 4. In particular, this figure shows the modelled w versus w obtained from the observations for the same data as used in Figure A.3. Here, w obtained from the observations was calculated by replacing the modelled velocity in Equation (6) by the observed velocity. The second step focuses on the inner contributions $(U^+)_{in} = U^+ - U_3^+$ and $(S^+)_{in} = S^+ - S_3^+$ of the velocity and its gradient. In particular, Figure 5(a) shows the modelled versus observed velocity obtained from DNS for the three flows and Reynolds numbers considered before. Figure 5(b–d) show corresponding velocity gradients for the highest Reynolds numbers of these DNS data for all three flows (corresponding curves at lower Reynolds numbers look very similar).

The evaluation of modelled wake physics in Figure 4 reflects the same data scattering seen in Figure A.3. The basic observation is that the observations fluctuate about the corresponding 1:1 lines, i.e. the wake physics is correctly reflected by the corresponding models. Given the fluctuations involved here, an evaluation of modelled versus observed gradients of w does not appear to be meaningful. Another view point of this question is to ask how the wake physics in channel/pipe flow and the TBL are related. This question is addressed in
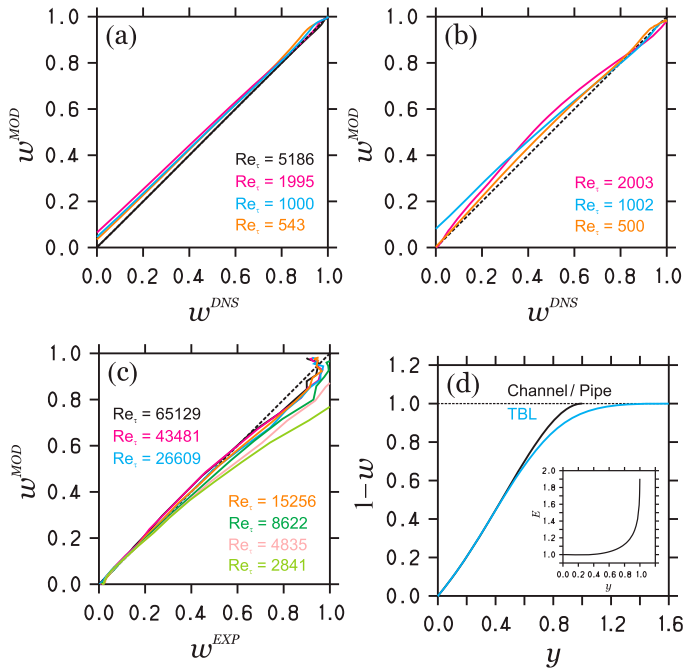
Figure 4. DNS (w^{DNS}) and experimental (w^{EXP}) wake functions w are shown versus modelled (w^{MOD}) wake functions for the given Reynolds numbers in (a), (b), and (c) for channel flow, pipe flow, and the TBL, respectively. The DNS and experimental wake functions were obtained by replacing the modelled velocity by the velocity given by DNS data of Lee and Moser [64,65], DNS data of Chin et al. [66], and Pitot experimental data of Vallikivi et al. [72]), respectively. In all plots, black dashed lines show 1:1 lines. Figure (d) shows the modelled $1-w$ for channel/pipe flow and the TBL, respectively. The horizontal black dashed line shows $1-w=1$. The inset shows the domain expansion factor $E = d_w/y$.

terms of Figure 4(d) which shows the wake flow transition probability $F_w = 1 - w$, which varies between zero and one, for channel/pipe flow and the TBL, respectively. We see the same mechanism of wake physics, which is only slightly modified by the domain size effect (a bounded domain for channel/pipe flow versus an unbounded domain for the TBL). It is worth noting that the collapse of $F_{w,CP}$ and $F_{w,BL}$ for relatively small y values provides significant support for the reflection of wake physics by these models.

A better understanding of flow effects seen in Figure 4(d) can be obtained in the following way. It is obvious that the TBL $F_{w,BL}$ is very similar to the channel/pipe $F_{w,CP}$, but the transition happens at higher wall distances. So what is the wall distance d_w such that $w_{BL}(d_w) = w_{CP}(y)$? According to $w_{BL}(d_w) = w_{CP}(y)$, this wall distance $d_w \geq y$ can be obtained as solution of the equation $d_w(0.9 + d_w + 1.09d_w^2) = -\ln w_{CP}(y)$. A simple way to solve this cubic equation in d_w is to solve the quadratic equation $d_w^2 + 0.9d_w = -\ln w_{CP}(y) - 1.09d_w^3$ iteratively starting with $d_w = y$ in the d_w^3 term. The solution quickly converges if the d_w^3 term in the quadratic equation is updated by replacing d_w by the mean value of the new and old d_w values. The result $E = d_w/y$ is shown in the inset in Figure 4(d). This plot demonstrates that the transition to the asymptotic wake function Ky is the same in all three flows with the exception that it happens in the TBL at higher wall distances because of the unbounded domain (there is no 'pressure' imposed by a bounded domain).
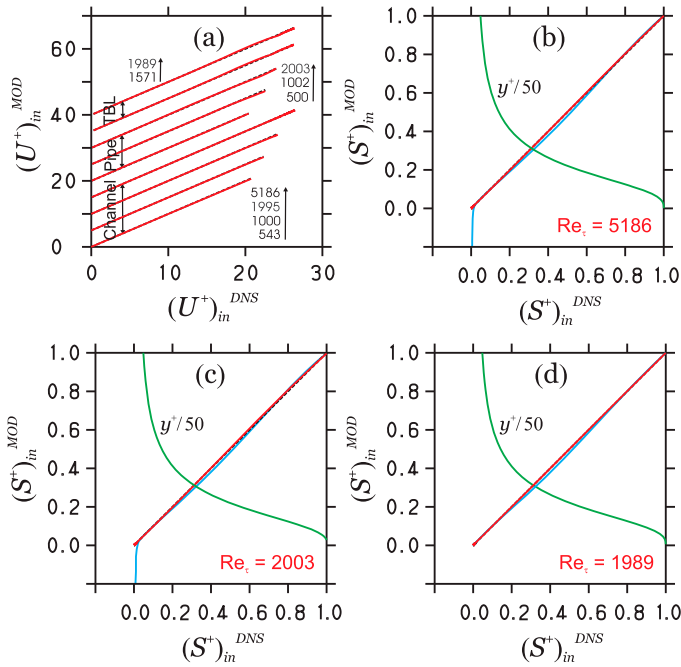
Figure 5. Figure (a) shows the modelled (superscript MOD) and DNS (superscript DNS) inner velocity $(U^+)_{in} = U^+ - U_3$ for channel flow, pipe flow, and the TBL, respectively, for the given Re_τ by red lines. Data at different Re_τ are moved up by $+5$. Figures (b), (c), and (d) show the corresponding shear rate $(S^+)_{in} = S^+ - S_3$ (red lines) for channel flow, pipe flow, and the TBL, respectively, for the given Re_τ. Corresponding cyan lines show corresponding predictions of Monkewitz's velocity model [36]. In all plots, black dashed lines show 1:1 lines, and green lines show $y^+/50$.

The factor $1 \leq E \leq 1.9$ will be referred to below as domain expansion factor to refer to the expanding TBL. The deviation of E from one over a significant portion of the flow field indicates the long-range influence of the domain length.

With respect to inner velocity variations, the evaluation of the model physics by Figure 5 provides impressive support for the correctness of modelled physics. The modelled versus observed velocity plot in Figure 5(a) shows that there is basically no deviation (and in particular no systematic) from the 1:1 lines for all three flows considered. The $(S^+)_{in}$ plots of the velocity derivative in Figure 5(b–d) lead to the same conclusion: the velocity model accurately reflects the physics.

3.4. Comparisons with empirical velocity models

The ability of the velocity model presented to satisfy the criteria of veritable physics derived from observations is certainly not a general feature of other velocity models (designed on an empirical basis). For example, the model of Chauhan et al. [35] does not satisfy the first criterion (see the modelling of the wake component). In an attempt to overcome these issues, Monkewitz recently suggested an improved velocity model [36]. Figure 5(b–d) demonstrate the reflection of physics by this model by focusing on inner velocity variations. For channel and pipe flow, this model reflects physics incorrectly for small $(S^+)_{in}$,
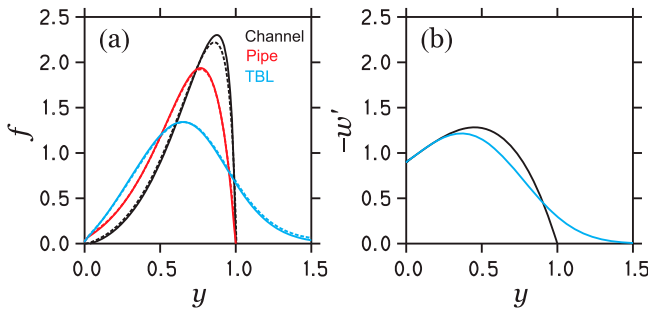
Figure 6. Figure (a) shows the PDF f for channel flow, pipe flow, and the TBL, respectively, for $Re_\tau = 500$ (dashed line) and $Re_\tau = 10^5$ (solid line). Figure (b) shows the PDF $-w'$ for channel/pipe flow and the TBL, respectively.

where the model predicts negative $(S^+)_{in}$. The reason for this is the consideration of differences between κ values used for the logarithmic inner velocity variation and κ values based on the friction law ($\Delta U^+_{log,Ch}$ and $\Delta U^+_{log,P}$ in reference [36]), see the explanations at the end of Appendix A.2. For all three flows, Monkewitz's model differs from the 1:1 line for $8 \leq y^+ \leq 27$, as may be seen by taking reference to the corresponding $y^+/50$ curves in Figure 5(b–d). Although the difference is relatively small, it indicates deficiencies regarding the correct reflection of physics.

A usual notion is that the physics of wake contributions is less clear than the physics of velocity variations in inner scaling. An improved insight into the mechanism of wake contributions was recently offered [90]. By following this approach we introduce the probability $F = U^+_3/(U^+_\infty - U^+_1 - U^+_2)$. By using F, the mean velocity model reads

$$U^+ = (U^+_1 + U^+_2)(1 - F) + FU^+_\infty. \tag{8}$$

This equation reflects the transition between $U^+_1 + U^+_2$ and U^+_∞. Given F, we can define a probability density function (PDF) by $f = dF/dy$. In Krug et al. [90], the PDF f had to be assumed and parametrised: for all the three flows considered here, f was assumed to be only a function of y, normally distributed and combined with parameters fitted to experiments. By using the velocity model presented here, the PDF f can be calculated from the model. It is shown in Figure 6(a) for the three flows considered and different Reynolds numbers. It appears that these PDFs are affected by the Reynolds number and not normally distributed. The TBL PDF has a shape that is relatively similar to a normal distribution. The corresponding channel and pipe flow PDFs cannot be normally distributed because of their bounded domain (bounded by zero and one). However, it turns out that Reynolds number effects have a relatively small influence on the PDF. In particular, the three PDFs rapidly converge to their asymptotic PDF, which is determined by $F_\infty = ln(w + Ky)/ln(Ky)$.

With respect to the latter discussion it is of interest to compare the PDF f with the PDF $-w'$ which follows from the probability $F_w = 1 - w$ for the onset of asymptotic wake variations. The corresponding plots are shown in Figure 6(b). The f PDFs are affected by the Reynolds number, U^+_∞ (via the flow considered), and the available domain in probability space. Figure 6(b) shows that the $-w'$ PDF is much more universal than f: it is unaffected by the Reynolds number, and the same for channel and pipe flow. The only influence that

is left is the domain in probability space, which leads to the modifications of the PDF $-w'$ for the TBL.

4. Implications

After presenting and validating the velocity model in Section 3, let us use the findings obtained to address the questions Q1 (mean velocity structure) in Section 4.1 and both Q2 (mean flow universality) and Q3 (consistency of log-law theory) in Section 4.2.

### 4.1. Mean flow structure: deterministic and probabilistic views

The velocity model Equation (6) was already discussed in Section 3.1, second paragraph. Let us prepare a more detailed discussion of the mean velocity structure in the following paragraphs by an identical rewriting of Equation (6),

$$U^+ - U_\infty^+ = \frac{1}{\kappa} \ln (K_* Y). \tag{9}$$

Here, $K_* = y_\kappa^{-1} e^{\sigma \kappa U_{1\infty}^+ - C}$ is introduced, which differs from $K = y_\kappa^{-1} e^{\kappa U_{1\infty}^+ - C}$ by the appearance of σ, and Y is introduced. The latter two variables, Y and σ, are defined by the expressions

$$Y = y_\kappa Re_\tau^{-1} e^{\kappa (U_1^+ - U_{1\infty}^+)} \left(1 + Hy^+/y_\kappa\right), \qquad \sigma = 1 - \ln \left(1 - F_w + Ky\right) /(\kappa U_{1\infty}^+), \tag{10}$$

which involve $F_w = 1 - w$. Here, $Re_\tau Y$ is only a function of y^+ and σ is only a function of y. Plots of Y and σ are shown in Figure 7. We see that Y and σ are well characterised by their log-law representatives y and 1, respectively. There are deviations, see the inset of Figure 7(a,b), but these deviations are relatively small. In particular, the relative error e_Y of $Re_\tau Y$ compared to y^+ is $e_Y \leq (1, 0.1)\%$ for $y^+ = (1700, 10^4)$. The comparison of Equation (9) with the velocity defect law Equation (2) shows, that the mean velocity has, basically, a log-law structure. However, this finding does not mean that wall damping and wake effects (represented by deviations of Y and σ from y and 1) have insignificant effects.
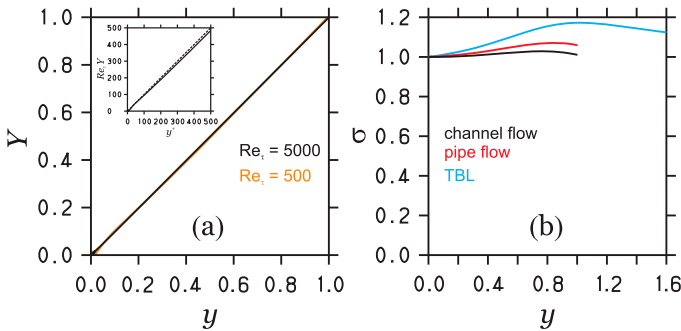
Figure 7. The functions Y and σ defined by Equation (10) are shown in (a) for the given Re_τ and in (b) for the three flows considered, respectively. The inset in (a) shows $Re_\tau Y$ versus y^+ (solid line) compared to the 1:1 line (dashed line).

As shown in reference [44], these effects essentially determine the structure of turbulence related to the mean flow (e.g. the turbulence production and turbulent viscosities). Thus, an accurate representation of these effects is clearly relevant.

A probabilistic view point is helpful to obtain a deeper understanding of the mean flow structure. To prepare this discussion we introduce

$$F_M(U^+) = \frac{e^{\kappa U^+} - 1}{e^{\kappa U_\infty^+} - 1} = \alpha \left[e^{\kappa(U^+ - U_\infty^+)} - 1 \right] + 1 = \alpha \left[K_* Y - 1 \right] + 1, \tag{11}$$

which represents the distribution function for the distribution of mean velocities along the wall-normal direction [91–95]. Its PDF $f_M(U^+) = dF_M/dU^+$ is given by

$$f_M(U^+) = \frac{\kappa e^{\kappa U^+}}{e^{\kappa U_\infty^+} - 1} = \alpha \kappa e^{\kappa(U^+ - U_\infty^+)} = \alpha \kappa K_* Y. \tag{12}$$

The terms in Equations (11) and (12) represent identical rewritings that involve $\alpha = (1 - e^{-\kappa U_\infty^+})^{-1} = (1 - 1/(Re_\tau e^C))^{-1}$, and Equation (9) is used. The normalisation constraint for f_M recovers the definition of α.

The PDF f_M represents a statistically most-likely PDF that maximises the related entropy [51,91,92,94,96]. The parameter κ that appears in Equations (11) and (12) can be chosen in accordance with global conditions on f_M [96]. One global condition is given by the mean $\int_0^{U_\infty^+} U^+ f_M \, dU^+ = \alpha U_\infty^+ - \kappa^{-1}$ over the velocity distribution Equation (12). Another such global condition is given by the entropy $S_E = 1 - \ln \kappa + \kappa U_\infty^+ (1 - \alpha) - \ln \alpha$, which follows from Equation (12) combined with the definition of the entropy $S_E = -\int_0^{U_\infty^+} \ln(f_M) f_M \, dU^+$. For the case considered, the definition of both the mean and entropy S_E is simply a matter of convenience. Therefore, we continue here to identify κ to be the von Kármán constant as used before. Then, for the flows and range $Re_\tau \geq 500$ considered, the effect of $Re_\tau^{-1} e^{-C}$ in α is smaller than 0.025%. Thus, we have $\alpha = 1$, which implies $F_M = K_* Y$, $f_M = \kappa K_* Y$, and $S_E = 1 - \ln \kappa$. We observe that the von Kármán constant $\kappa = e^{1 - S_E}$ represents an entropy measure.

The expressions obtained in the preceding paragraph for the entropy S_E and distribution function F_M do not involve any specification of a mean flow model. Which implications for the mean flow structure arise from S_E and F_M? A first implication is that the von Kármán constant needs to be the same for all three flows considered because the entropy needs to be the same (the use of different κ values for different flows would result in different entropies, which is unphysical). A second implication is that F_M should be a linear function of y in absence of boundary effects (wall damping and wake effects): all velocity values need to be equally likely in a region unaffected by boundary effects. These requirements are satisfied by $F_M = K_* Y$, which turns into $F_M = Ky$ in absence of boundary effects (see the discussion of σ and Y above). In addition to these requirements, $F_M = K_* Y$ correctly involves wall damping and wake effects as demonstrated above (it is worth noting that F_M curves show a maximum $F_M = 1$ for all three flows considered). The relevant result of this discussion is the conclusion that the constraints of equal entropies and equally likely velocity values in a region unaffected by boundary effects impose a universal log-law structure of the mean flow.

Another relevant observation is the following. The distribution function $F_M = K_* Y$ is a product of K_* (which depends only on y), $Re_\tau Y$ (which depends only y^+), and

Re_τ^{-1}. This means there is no interaction between velocity variations in response to inner and outer scaling. A more comprehensive discussion of implications of this fact can be found in reference [44] in conjunction with a discussion of active and inactive turbulence interactions.

4.2. Mean flow universality and log-law theory

How universal are the mean flow equations presented in Section 4.1, and how universal is the log-law theory? The latter questions are the concern of intense recent discussions. For example, Monkewitz [36] suggested the following picture. Velocity variations in inner scaling show an internal discrepancy for channel and pipe flow with respect to local and global log-law formulations (characterized by different κ values). Only the TBL is consistent in this regard. The logarithmic variations of the three flows considered are different. Hence, velocity variations in outer scaling are different for the three flows considered without any common component. So this picture corresponds to the view that the three flows have not much in common regarding their structure and there are differences between local and global log-law formulations with respect to channel and pipe flow. This would mean that the structure of different but similar wall-bounded flows is different. The results reported here with respect to these questions support a different view.

First, regarding the mean flow universality, we observe the following. Via the wake contribution $U_3^+ = -\kappa^{-1} \ln(1 - F_w + Ky)$, the influence of the flow considered is limited to the constant $K = y_\kappa^{-1} e^{\kappa U_{1\infty}^+ - C}$ and the domain expansion factor E, which moves the transition probability F_w for the TBL to higher wall distances in response to the unbounded domain. In other words, F_w has the same variation for all three flows considered, the only difference regarding the TBL is that the transition is postponed. Thus, the influence of flow effects on the mean flow is limited to the minimum: the difference of having a bounded or unbounded domain, and the variation range of mean velocity values allowed by the geometry (which is reflected by K^{-1} [96]). Thus, the remaining velocity variations in inner scaling, U_1^+ and U_2^+, which include logarithmic variations, are the same for all three flows considered. Second, regarding the universality of log-law theory (see the discussion in Section 2), the results reported here do not indicate discrepancies of various log-law formulations. For the three flows, we find the same logarithmic inner-scaled velocity variations. There is no discrepancy between local logarithmic velocity variations and global friction law and bulk velocity variations.

5. Concluding remarks

The understanding of the mathematical physical mean flow structure of wall-bounded turbulent flows still faces open questions. Three questions (Q1-Q3, see the introduction) were considered here: the physical mean flow structure of wall-bounded flows, the universality of the mean flow, and the validity and consistency of log-law theory.

The latter questions were addressed for three canonical wall-bounded turbulent flows (channel flow, pipe flow, and the TBL) by using latest DNS and experimental data [64–77] at moderate and high Reynolds numbers, respectively. An analytical mean flow model was derived, which was demonstrated to be in excellent agreement with all DNS and experimental data applied. Specific emphasis was placed on the question of how accurately

the physics of wall-bounded turbulent flows is reflected by the analytical velocity model obtained. This question was addressed, first, by formulating criteria for veritable physics derived from observations, and, second, by demonstrating that the velocity model obtained satisfies these criteria.

Detailed answers to the Q1–Q3 questions considered were provided in Section 4. In short, the following answers were obtained.

(Q1) A probabilistic interpretation of the mean flow structure shows that the physical constraints of equal entropies and equally likely mean velocity values in a region unaffected by boundary effects impose a universal log-law structure. The distribution function of mean velocity values consists of independent modes that account of inner-scaled and outer-scaled velocity variations, i.e. there is no interaction between these variations. The latter observation reflects the interaction of active and inactive turbulence described in reference [44].

(Q2) The structure of wall-bounded flows is much more universal than previously expected. Flow effects are limited to the minimum: the difference of having a bounded or unbounded domain, and the variation range of mean velocity values allowed by the geometry. The three flows considered have the same entropy S_E because of the universal value of the von Kármán constant $\kappa = e^{1-S_E}$.

(Q3) The results reported here do not indicate any discrepancies of different log-law formulations: for the three flows, we find the same logarithmic velocity variations in inner scaling, and there is no discrepancy between local logarithmic velocity variations, and global friction law and global bulk velocity variations. It is worth noting that these conclusions resolve issues regarding these questions pointed out recently on the basis of previous data [36].

It is worth noting that the analysis presented here does not deal with two obvious and relevant extensions: the inclusion of turbulence statistics related to the mean flow, and the discussion of implications of results obtained here with respect to the asymptotic physics at extreme Re_τ. Several questions related to the latter extensions (e.g. regarding the self-similar asymptotic flow structure, the convergence of flow statistics to the asymptotic state, and the physical flow organisation at extreme Re_τ) are the concern of a companion paper [44].

References

[1] von Kármán T. Mechanische Ähnlichkeit und Turbulenz [Mechanical similitude and turbulence]. In Nachrichten der Akademie der Wissenschaften Göttingen, Math.-Phys. Klasse; 1930. p. 58–76. [Technical memorandum N611,National Advisory Committee for Aeronautics,Washington; 1931].

[2] Pope SB. Turbulent flows. Cambridge: Cambridge University Press; 2000.

[3] Marusic I, McKeon BJ, Monkewitz PA, et al. Wall-bounded turbulent flows at high Reynolds numbers: recent advances and key issues. Phys Fluids. 2010;22(6):065103/1–065103/24.

[4] Smits AJ, McKeon BJ, Marusic I. High-Reynolds number wall turbulence. Annu Rev Fluid Mech. 2011;43(1):353–375.

[5] Jiménez J. Near-wall turbulence. Phys Fluids. 2013;25(10):101302/1–101302/28.

[6] Wallace JM. Highlights from 50 years of turbulent boundary layer research. J Turbul. 2013;13(53):1–70.

[7] Zagarola MV, Perry AE, Smits AJ. Log laws or power laws: the scaling in the overlap region. Phys Fluids. 1997;9(7):2094–2100.

[8] Buschmann MH, Gad el Hak M. Generalized logarithmic law and its consequences. AIAA J. 2003a;41(1):40–48.

[9] Buschmann MH, Gad el Hak M. Debate concerning the mean-velocity profile of a turbulent boundary layer. AIAA J. 2003b;41(4):565–572.

[10] Buschmann MH, Gad el Hak M. Recent developments in scaling of wall-bounded flows. Prog Aerospace Sci. 2007;42(5-6):419–467.

[11] Buschmann MH, Gad el Hak M. Evidence of nonlogarithmic behavior of turbulent channel and pipe flow. AIAA J. 2009;47(3):535–541.

[12] Buschmann MH, Gad el Hak M. Turbulent boundary layers: is the wall falling or merely wobbling?Acta Mech. 2011;218(3–4):309–318.

[13] George WK. Is there a universal log law for turbulent wall-bounded flows? Phil Trans R Soc A. 2007;365(1852):789–806.

[14] Davidson PA. Turbulence: an introduction for scientists and engineers. Oxford: Oxford University Press; 2004.

[15] Morrison JF. The interaction between inner and outer regions of turbulent wall-bounded flow. Phil Trans R Soc A. 2007;365(1852):683–698.

[16] Oberlack M. A unified approach for symmetries in plane parallel turbulent shear flows. J Fluid Mech. 2001;427:299–328.

[17] Bernardini M, Pirozzoli S, Orlandi P. Velocity statistics in turbulent channel flow up to $Re_\tau =$ 4000. J Fluid Mech. 2014;742:171–191.

[18] Townsend AA. The structure of turbulent shear flow. 2nd ed. Cambridge: Cambridge University Press; 1976.

[19] Marusic I, Monty JP, Hultmark M, et al. On the logarithmic region in wall turbulence. J Fluid Mech. 2013;716:R3/1–R3/11.

[20] Woodcock JD, Marusic I. The statistical behaviour of attached eddies. Phys Fluids. 2015;27(1):015104/1–015104/24.

[21] Yang XIA, Marusic I, Meneveau C. Hierarchical random additive process and logarithmic scaling of generalized high order, two-point correlations in turbulent boundary layer flow. Phys Rev Fluids. 2016;1:024402/1–024402/15.

[22] Barenblatt GI. Scaling, self-similarity and intermediate asymptotics. Cambridge: Cambridge University Press; 1996.

[23] Barenblatt GI. Scaling laws for fully developed turbulent shear flows. Part 1: basic hypotheses and analysis. J Fluid Mech. 1993;248:513–520.

[24] Barenblatt GI, Prostokishin VM. Scaling laws for fully developed turbulent shear flows. Part 2: processing of experimental data. J Fluid Mech. 1993;248:521–529.

[25] Kazakov KA. The mean velocity profile of near-wall turbulent flow: is there anything in between the logarithmic and power laws? J Turbul. 2016;17(11):1015–1047.

[26] Klewicki J, Fife P, Wei T. On the logarithmic mean profile. J Fluid Mech. 2009;638: 73–93.

[27] Bailey SCC, Vallikivi M, Hultmark M, et al. Estimating the value of von Kármán's constant in turbulent pipe flow. J Fluid Mech. 2014;749:79–98.

[28] Wu Y, Chen X, She Z-S, et al. On the Karman constant in turbulent channel flow. Phys Scr. 2013;T155:014009/1–014009/4.

[29] Luchini P. Universality of the turbulent velocity profile. Phys Rev Lett. 2017;118(22):224501/1–224501/4.

[30] Musker AJ. Explicit expression for the smooth wall velocity distribution in a turbulent boundary layer. AIAA J. 1979;17(6):655–657.

[31] Chauhan KA, Nagib HM, Monkewitz PA. On the composite logarithmic profile in zero pressure gradient turbulent boundary layers. 45th AIAA aerospace sciences meeting and exhibit, AIAA Paper 07-532, Reno, NV, 2007.

[32] Monkewitz PA, Chauhan KA, Nagib HM. Self-consistent high-Reynolds-number asymptotics for zero-pressure-gradient turbulent boundary layers. Phys Fluids. 2007;19(11):115101/1–115101/12.

[33] Nagib HM, Chauhan KA. Variations of von Kármán coefficient in canonical flows. Phys Fluids. 2008;20(10):101518/1–101518/10.

[34] Monkewitz PA, Chauhan KA, Nagib HM. Comparison of mean flow similarity laws in zero pressure gradient turbulent boundary layers. Phys Fluids. 2008;20(10):105102/1–105102/16.

[35] Chauhan KA, Monkewitz PA, Nagib HM. Criteria for assessing experiments in zero pressure gradient boundary layers. Fluid Dyn Res. 2009;41:021404/1–021404/23.

[36] Monkewitz PA. Revisiting the quest for a universal log-law and the role of pressure gradient in canonical wall-bounded turbulent flows. Phys Rev Fluids. 2017;2(9):094602/1–094602/17.

[37] Coleman G, Kim J, Moser R. A numerical study of turbulent supersonic isothermal-wall channel flow. J Fluid Mech. 1995;305:159–183.

[38] Huang P, Coleman G, Bradshaw P. Compressible turbulent channel flows: DNS results and modeling. J Fluid Mech. 1995;305:185–218.

[39] Foysi H, Sarkar S, Friedrich R. Compressibility effects and turbulence scalings in supersonic channel flow. J Fluid Mech. 2004;509:207–216.

[40] Ghosh S, Foysi H, Friedrich R. Compressible turbulent channel and pipe flow: similarities and differences. J Fluid Mech. 2010;648:155–181.

[41] Li X-L, Fu D-X, Ma Y-W, et al. Direct numerical simulation of compressible turbulent flows. Acta Mech Sin. 2010;26(6):795–806.

[42] Zhang Y-S, Bi W-T, Hussain F, Li X-L, She Z-S. Mach-number-invariant mean-velocity profile of compressible turbulent boundary layers. Phys Rev Lett. 2012;109(5):054502/1–054502/4.

[43] Modesti D, Pirozzoli S. Reynolds and Mach number effects in compressible turbulent channel flow. Int J Heat Fluid Flow. 2016;59(6):33–49.

[44] Heinz S. On mean flow universality of turbulent wall flows. II. Asymptotic flow analysis. (submitted), 2019;20(2):174–193.

[45] Kalitzin G, Medic G, Templeton JA. Wall modeling for LES of high Reynolds number channel flows: what turbulence information is retained? Comput Fluids. 2008;37:809–815.

[46] Pantano C, Pullin DI, Dimotakis PE, Matheou G. LES approach for high Reynolds number wall-bounded flows with application to turbulent channel flow. J Comput Phys. 2008;227:9271–9291.

[47] Chung D, Pullin DI. Large-eddy simulation and wall modelling of turbulent channel flow. J Fluid Mech. 2009;631:281–309.

[48] Chung D, McKeon BJ. Large-eddy simulation of large-scale structures in long channel flow. J Fluid Mech. 2010;661:341–364.

[49] Chen S, Xia Z, Pei S, et al. Reynolds-stress-constrained large-eddy simulation of wall-bounded turbulent flows. J Fluid Mech. 2012;703:1–28.

[50] Yang XIA, Sadique J, Mittal R, Meneveau C. Integral wall model for large eddy simulations of wall-bounded turbulent flows. Phys Fluids. 2015;27(2):025112/1–025112/32.

[51] Heinz S. Statistical mechanics of turbulent flows. Berlin, Heidelberg, New York, Tokyo: Springer-Verlag; 2003.

[52] Heinz S. Unified turbulence models for LES and RANS, FDF and PDF simulations. Theor Comput Fluid Dyn. 2007;21(2):99–118.

[53] Heinz S. Realizability of dynamic subgrid-scale stress models via stochastic analysis. Monte Carlo Methods Appl. 2008;14(4):311–329.

[54] Heinz S, Gopalan H. Realizable versus non-realizable dynamic subgrid-scale stress models. Phys Fluids. 2012;24(11):115105/1–115105/23.

[55] Gopalan H, Heinz S, Stöllinger M. A unified RANS-LES model: computational development, accuracy and cost. J Comput Phys. 2013;249:249–279.

[56] Mokhtarpoor R, Heinz S, Stoellinger M. Dynamic unified RANS-LES simulations of high Reynolds number separated flows. Phys Fluids. 2016;28(9):095101/1–095101/36.

[57] Mokhtarpoor R, Heinz S. Dynamic large eddy simulation: stability via realizability. Phys Fluids. 2017;29(10):105104/1–105104/22.

[58] Reichardt H. Vollständige Darstellung der turbulenten Geschwindigkeitsverteilung in glatten Leitungen. ZAMM - J Appl Math Mech. 1951;31(7):208–219.

[59] Afzal N, Seena A, Bushra A. Power law velocity profile in fully developed turbulent pipe and channel flows. ASCE J Hydraul Eng. 2007;133(9):1080–1086.

[60] Panton RL. Composite asymptotic expansions and scaling wall turbulence. Phil Trans R Soc A. 2007;365(1852):733–754.

[61] Silva Freire AP. The persistence of logarithmic solutions in turbulent boundary layer systems. J Braz Soc Mech Sci Eng. 2016;38(5):1359–1399.

[62] Nickels TB. Inner scaling for wall-bounded flows subject to large pressure gradients. J Fluid Mech. 2004;521:217–239.

[63] Guo J. Eddy viscosity and complete log-law for turbulent pipe flow at high Reynolds numbers. J Hydraulic Res. 2017;55(1):27–39.

[64] Lee M, Moser RD. Direct numerical simulation of turbulent channel flow up to $Re_\tau = 5200$. J Fluid Mech. 2015;774:395–415.

[65] Available from: http://turbulence.ices.utexas.edu, 2016a.

[66] Chin C, Monty JP, Ooi A. Reynolds number effects in DNS of pipe flow and comparison with channels and boundary layers. Int J Heat Fluid Flow. 2014;45:33–40.

[67] Sillero JA, Jiménez J, Moser RD. One-point statistics for turbulent wall-bounded flows at Reynolds numbers up to $\delta^+ \approx 2000$. Phys Fluids. 2013;25(10):105102/1–105102/16.

[68] Available from: http://torroja.dmt.upm.es/turbdata/blayers, 2016b.

[69] Schultz MP, Flack KA. Reynolds-number scaling of turbulent channel flow. Phys Fluids. 2013;25(2):025104/1–025104/13.

[70] Hultmark M, Vallikivi M, Bailey SCC, et al. Logarithmic scaling of turbulence in smooth-and rough-wall pipe flow. J Fluid Mech. 2013;728:376–395.

[71] Available from: https://smits.princeton.edu/superpipe-turbulence-data, 2016.

[72] Vallikivi M, Hultmark M, Smits AJ. Turbulent boundary layer statistics at very high Reynolds number. J Fluid Mech. 2015;779:371–389.

[73] Lozano-Durán A, Jiménez J. Effect of the computational domain on direct simulations of turbulent channels up to $Re_\tau = 4200$. Phys Fluids. 2014;26(1):011702/1–011702/8.

[74] Available from: http://torroja.dmt.upm.es/channels/data, 2016c.

[75] Ahn J, Lee JH, Lee J, Kang J, Sung HJ. Direct numerical simulation of a 30R long turbulent pipe flow at $Re_\tau = 3008$. Phys Fluids. 2015;27(6):065110/1–065110/14.

[76] Schlatter P, Örlü R. Assessment of direct numerical simulation data of turbulent boundary layers. J Fluid Mech. 2010;659:116–126.

[77] Available from: http://www.mech.kth.se/ pschlatt/data/readme.html, 2016d.

[78] Millikan CB. A critical discussion of turbulent flows in channels and circular tubes. In Proceedings of the 5th international congress of applied mechanics. New York: Wiley; 1938. p. 386–392.

[79] Jiménez J, Moser RD. What are we learning from simulating wall turbulence? Phil Trans R Soc A. 2007;365(1852):715–732.

[80] Bailly C, Comte-Bellot G. Turbulence. Cham, Heidelberg, New York, Dordrecht, London: Springer; 2015.

[81] Pullin DI, Inoue M, Saito N. On the asymptotic state of high Reynolds number, smooth-wall turbulent flows. Phys Fluids. 2013;25(1):015116/1–015116/9.

[82] Coles D. The law of the wake in the turbulent boundary layer. J Fluid Mech. 1956;1(2):191–226.

[83] Zagarola MV, Smits AJ. Mean-flow scaling of turbulent pipe flow. J Fluid Mech. 1998;373:33–79.

[84] McKeon BJ, Li J, Jiang W, et al. Further observations on the mean velocity distribution in fully developed pipe flow. J Fluid Mech. 2004;501:135–147.

[85] Morrison JF, McKeon BJ, Jiang W, et al. Scaling of the streamwise velocity component in turbulent pipe flow. J Fluid Mech. 2004;508:99–131.

[86] Hultmark M, Vallikivi M, Bailey SCC, et al. Turbulent pipe flow at extreme Reynolds numbers. Phys Rev Lett. 2012;108:094501.

[87] Vallikivi M. Wall-bounded turbulence at high Reynolds numbers [PhD thesis]. Princeton University; 2014.

[88] Yamamoto Y, Tsuji Y. Numerical evidence of logarithmic regions in channel flow at $Re_\tau = 8000$. Phys Rev Fluids. 2018;3(1):012602/1–012602/10.

[89] Lundgren TS. Asymptotic analysis of the constant pressure turbulent boundary layer. Phys Fluids. 2007;19(5):055105/1–055105/17.

[90] Krug D, Philip J, Marusic I. Revisiting the law of the wake in wall turbulence. J Fluid Mech. 2017;811:421–435.

[91] Chiu C-L. Entropy and probability concepts in hydraulics. J Hydraul Eng. 1987;113(5):583–599.

[92] Chiu C-L. Entropy and 2-D velocity distribution in open channels. J Hydraul Eng. 1988;114(7):738–756.

[93] Dingman SL. Probability distribution of velocity in natural channel cross sections. Water Resour Res. 1989;25(3):509–518.

[94] Fontana N, Marini G, De Paola F, Experimental assessment of a 2-D entropy-based model for velocity distribution in open channel flow. Entropy. 2013;15(3):988–998.

[95] Moramarco T, Dingman SL. On the theoretical velocity distribution and flow resistance in natural channels. J Hydrol. 2017;555:777–785.

[96] Heinz S. Mathematical modeling. 1st ed. Heidelberg, Dordrecht, London, New York: Springer-Verlag; 2011.

[97] Buschmann MH, Indinger T, Gad el Hak M, Near-wall behavior of turbulent wall-bounded flows. Int J Heat Fluid Flow. 2009;30(5):993–1006.

[98] Inoue M, Pullin DI. Large-eddy simulation of the zero-pressure-gradient turbulent boundary layer up to $Re_\theta = O(10^{12})$. J Fluid Mech. 2011;686:507–533.

[99] Fernholz HH, Finley PJ. The incompressible zero-pressure gradient turbulent boundary layer: an assessment of the data. Prog Aerosp Sci. 1996;32(4):245–311.

[100] Monty JP, Hutchins N, Ng HCH, et al. A comparison of turbulent pipe, channel and boundary layer flows. J Fluid Mech. 2009;632:431–442.

[101] Ng HCH, Monty JP, Hutchins N, et al. Comparison of turbulent channel and pipe flows with varying Reynolds number. Exp Fluids. 2011;51:1261–1281.

[102] Hoyas S, Jiménez J. Scaling of velocity fluctuations in turbulent channels up to $Re_\tau = 2003$. Phys Fluids. 2006;18(1):011702.

[103] Thais L, Mompean G, Gatski T. Spectral analysis of turbulent viscoelastic and Newtonian channel flow. J Non-Newtonian Fluid Mech. 2013;200(10):165–176.

[104] Zagarola MV, Smits AJ. Scaling of the mean velocity profile for turbulent pipe flow. Phys Rev Lett. 1997;78(2):239–242.

Appendices

Appendix A. Model Development

The mean velocity model development is presented here in four steps. A velocity model for the inner layer is presented in Appendix A.1, the friction law is presented in Appendix A.2, wake layer effects are added in Appendix A.3. The outer boundary conditions are considered in the Supplementary Material.
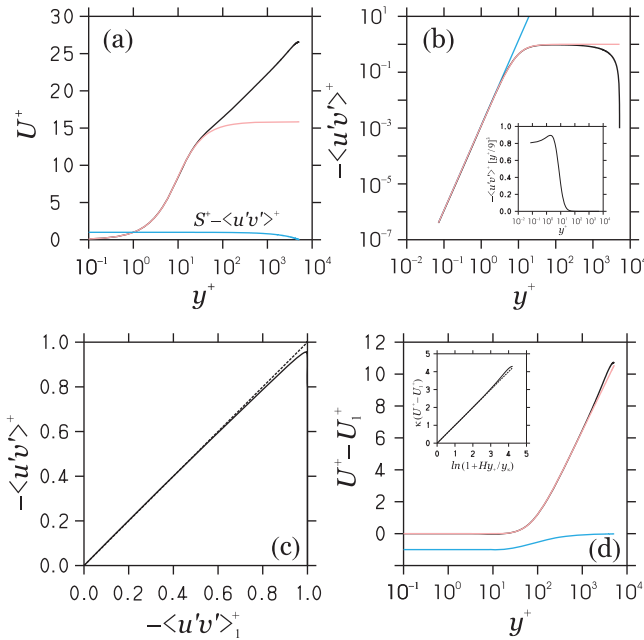
A.1   Model Development I: Inner Layer

Let us consider first the idea of deriving a universal scaling in y^+ for the mean streamwise velocity. Figures A.1a, b show the mean streamwise velocity U^+ and Reynolds shear stress $\langle u'v' \rangle^+$ (u' and v' refer to streamwise and wall-normal velocity fluctuations and the brackets indicate a Reynolds average) obtained from the channel flow DNS data of Lee & Moser [64, 65] for the highest Reynolds number case $Re_\tau = 5186$. The variations of U^+ and $\langle u'v' \rangle^+$ are related to each other by the momentum equation $S^+ - \langle u'v' \rangle^+ = 1 - y^+/Re_\tau$, which is satisfied by all Lee & Moser channel flow DNS data [64, 65] considered here with an inaccuracy of less than 0.23% (see reference [44]). These curves indicate two basic mechanisms: a U^+ variation implied by the damping of vertical velocity fluctuations in the viscous sublayer followed by a variation $U^+ \propto ln\, y^+$. The most promising approach to describe the variation of U^+ in the inner layer is to take advantage of the simple variations $ln(-\langle u'v' \rangle^+) \propto ln\, y^+$ and $U^+ \propto ln\, y^+$ in conjunction with $S^+ - \langle u'v' \rangle^+ = 1 - y^+/Re_\tau$. This approach will be applied in the following of this Appendix A.1 by reducing $S^+ - \langle u'v' \rangle^+ = 1 - y^+/Re_\tau$ to $S^+ - \langle u'v' \rangle^+ = 1$. This corresponds to a sequential development of the velocity model: wake effects that scale in y will be added below (see Appendix A.3) to contributions in inner scaling y^+ considered here. The validity of this approach is supported by means of Fig. A.1a: it may be seen that $S^+ - \langle u'v' \rangle^+ = 1$ represents a very accurate approximation except in the wake region. With respect to deriving inner-scaled velocity components in this Sect. A.1, we will focus in the following on the analysis of the highly accurate (see Appendix A) channel flow DNS data of Lee & Moser [64, 65] for the highest Reynolds number case $Re_\tau = 5186$.

The Reynolds shear stress $\langle u'v' \rangle^+$ is shown in Fig. A.1b in a double-logarithmic scale. It may be seen that the first stage (small y^+ values) can be very well described by a power law (a line in the double-logarithmic plot). After this stage, the DNS data show that $-\langle u'v' \rangle^+$ approaches a value very close to one, but not equal to one. This little deviation from one will be accounted for in the following by the consideration of additional contributions to U^+, see below. Thus, we consider

$$\langle u'v' \rangle_1^+ = -\left[\frac{(y^+/a)^{b/c}}{1 + (y^+/a)^{b/c}} \right]^c. \tag{A.1}$$

Here, the subscript one is used to refer to the fact that Eq. (A.1) represents only one contribution to the total Reynolds shear stress and mean streamwise velocity. An analysis of the $ln(-\langle u'v' \rangle^+) \propto ln\, y^+$ stage determines $a = 9$ and $b = 3.04$, and $c = 1.4$ follows from matching Eq. (A.1) to the DNS data in one point. Figure A.1b demonstrates the suitability of both $(y^+/9)^{3.04}$ in the first stage and Eq. (A.1) for the stage involving the leveling off of $-\langle u'v' \rangle^+$. It is of interest to observe that the scaling $(y^+/9)^{3.04}$ found here is very close to the classical near wall limit $-\langle u'v' \rangle^+ \propto y^{+3}$. The relation between $(y^+/9)^{3.04}$ and $-\langle u'v' \rangle^+ \propto y^{+3}$ is addressed in terms of the inset of Fig. A.1b, which shows DNS data of $-\langle u'v' \rangle^+/[y^+/9]^3$. This figure provides support for the existence of the classical near wall behavior $-\langle u'v' \rangle^+ \propto y^{+3}$ as an asymptotic limit for $y^+ \to 0$ (for $y^+ \le 0.1$), although it does not provide strict evidence (see also the corresponding discussion in [97]). It is of interest that this asymptotic limit is outside the range of available $Re_\tau = 5186$ DNS data. On the other hand, $(y^+/9)^{3.04}$ was derived here as a consequence of DNS data (for about $y^+ \le 2$). Thus, currently available data do not enable a strict inclusion of the classical near wall behavior, and, given the high accuracy of the mean velocity model presented here (see Appendix A), a strict asymptotic limit inclusion cannot be expected to improve the model performance. The structure of Eq. (A.1) reflects the two limiting trends, $(y^+/9)^{3.04}$ and one, and it is the most natural choice. However, in general,

Figure A.1. Model development I: channel flow DNS data of Lee & Moser [64, 65] for $Re_\tau = 5186$. Figure (a) shows DNS data for U^+ (black line) and $S^+ - \langle u'v'\rangle^+$ (cyan line) compared to U_1^+ (pink line) given by Eq. (A.8). Figure (b) shows DNS data for $-\langle u'v'\rangle^+$ (black line) compared to $(y^+/9)^{3.04}$ (cyan line) and $\langle u'v'\rangle_1^+$ (pink line) given by Eq. (A.1). Inset: DNS data of $-\langle u'v'\rangle^+/[y^+/9]^3$. Figure (c) shows $-\langle u'v'\rangle^+$ (black line) and $-\langle u'v'\rangle_1^+$ (black dashed line) versus $-\langle u'v'\rangle_1^+$ according to DNS. Figure (d) shows DNS data for $U^+ - U_1^+$ (black line) compared to U_2^+ according to Eq. (A.10) (pink line). The variation of $H-1$ according to Eq. (A.11) (cyan line) is also shown. Inset: $\kappa(U^+ - U_1^+)$ (black line) and $ln(1 + y^+H/y_\kappa)$ (black dashed line) versus $ln(1 + y^+H/y_\kappa)$.

there would be several ways to transition from one limit to the other. A way to confirm the suitability of the structure of Eq. (A.1) is to consider the relationship between $-\langle u'v'\rangle^+$ and $-\langle u'v'\rangle_1^+$ shown in Fig. A.1c in comparison to $-\langle u'v'\rangle_1^+$ versus $-\langle u'v'\rangle_1^+$. It may be seen that $-\langle u'v'\rangle_1^+$ determines the initial development of $-\langle u'v'\rangle^+$ extremely well.

By using the momentum equation $S^+ - \langle u'v'\rangle^+ = 1$, see the justification above, Eq. (A.1) implies

$$S_1^+ = 1 - \left[\frac{(y^+/a)^{b/c}}{1 + (y^+/a)^{b/c}} \right]^c, \tag{A.2}$$

where the subscript one refers to the shear produced by $\langle u'v'\rangle_1^+$. The integration of the latter expression then leads to the following expression for the mean velocity produced by S_1^+, which is referred to as U_1^+,

$$U_1^+ = \frac{ac}{b} \left[B_G\left(\frac{c}{b}, -\frac{c}{b}\right) - B_G\left(c + \frac{c}{b}, -\frac{c}{b}\right) \right]. \tag{A.3}$$

Here, the subscript G in $B_G()$ is defined by $G = (y^+/a)^{b/c}/[1 + (y^+/a)^{b/c}]$. The function $B_G()$ refers to the incomplete beta function, which is defined by

$$B_z(A, B) = \int_0^z s^{A-1}(1 - s)^{B-1} ds. \tag{A.4}$$
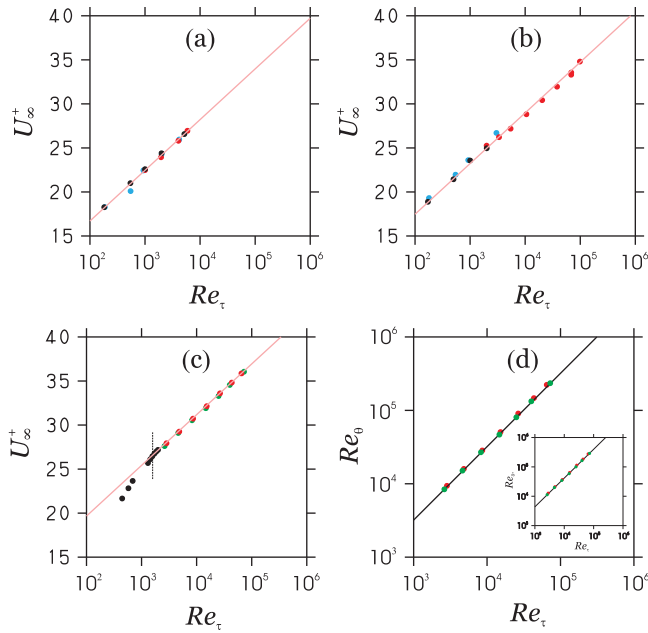
Figure A.2. Figure (a) shows U_∞^+ versus Re_τ according to channel flow DNS data of Lee & Moser [64, 65] (black dots), DNS data of Lozano-Durán & Jiménez [73, 74] (cyan dots), and experimental data of Schultz & Flack [69] (red dots). Figure (b) shows U_∞^+ according to pipe flow DNS data of Chin et al. [66] (black dots), DNS data of Ahn et al. [75] (cyan dots), and experimental data of Hultmark et al. [70, 71] (red dots). Figure (c) shows U_∞^+ according to TBL DNS data of Sillero et al. [67, 68]) (black dots), Pitot (red dots) and NSTAP (green dots) experimental data of Vallikivi et al. [72]). The dashed black line at $Re_\tau = 1571$ separates data at smaller Re_τ which suffer from a lack of recovery of the largest flow scales. The pink lines in (a), (b), (c) shows Eq. (3) combined with $C = (2.076, 2.382, 3.261)$, respectively. Figure (d) shows Re_θ versus Re_τ obtained from Pitot (red dots) and NSTAP (green dots) TBL experimental data [72]). The black line shows $Re_\theta = 3.2 Re_\tau$. The same is shown in the inset for $Re_{\delta*}$. The black line shows $Re_{\delta*} = 5 Re_\tau^{0.98}$.

The function $B_G()$ can be calculated by standard routines if the arguments of $B_G()$ are positive. To accomplish this we use the relation

$$B_z(A, B) = \frac{A+B}{B} B_z(A, B+1) - \frac{1}{B} z^A (1-z)^B. \tag{A.5}$$

The validity of Eq. (A.5) can be shown in the following way. First, we consider

$$B_z(A+1, B) + B_z(A, B+1) = \int_0^z s^{A-1}(1-s)^{B-1}(s+1-s)ds = B_z(A, B), \tag{A.6}$$

where the definition Eq. (A.4) of the incomplete beta function is applied. Second, we consider

$$\int_0^z \frac{ds^A(1-s)^B}{ds} ds = z^A(1-z)^B = AB_z(A, B+1) - BB_z(A+1, B). \tag{A.7}$$

By using Eq. (A.6) to replace $B_z(A+1, B)$ in Eq. (A.7) and solving for $B_z(A, B)$, we obtain Eq. (A.5). By using the latter relation we can write U_1^+ as

$$U_1^+ = a\left[cB_G\left(c+\frac{c}{b}, 1-\frac{c}{b}\right) + G^{\frac{c}{b}}(1-G)^{-\frac{c}{b}} - G^{c+\frac{c}{b}}(1-G)^{-\frac{c}{b}}\right]. \tag{A.8}$$
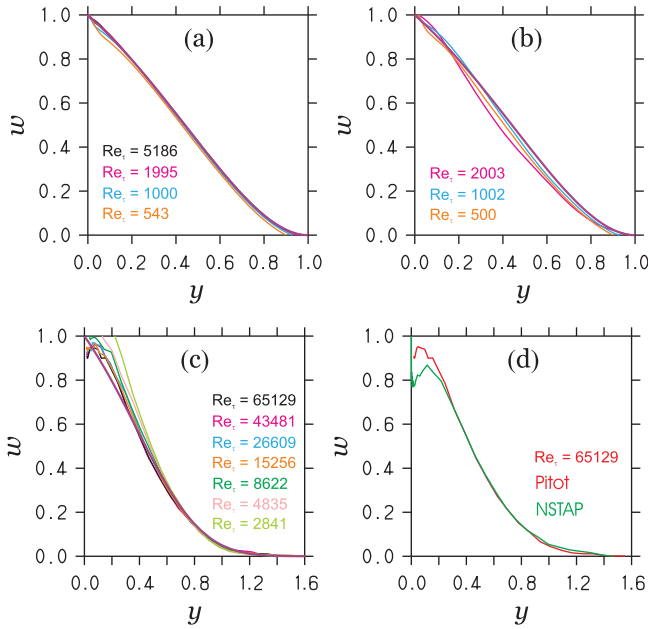
Figure A.3. Figures (a)-(c) show w according to channel flow DNS data of Lee & Moser [64, 65], pipe flow DNS data of Chin et al. [66], and Pitot TBL experimental data of Vallikivi et al. [72]), respectively, for the given Re_τ. The purple lines in (a) and (b) show Eq. (A.18). The purple line in (c) shows Eq. (A.19). Figure (d) shows w for the TBL for $Re_\tau = 65129$ obtained from Pitot (red line) and for $Re_\tau = 72526$ obtained from NSTAP (green line) experimental data [72]).
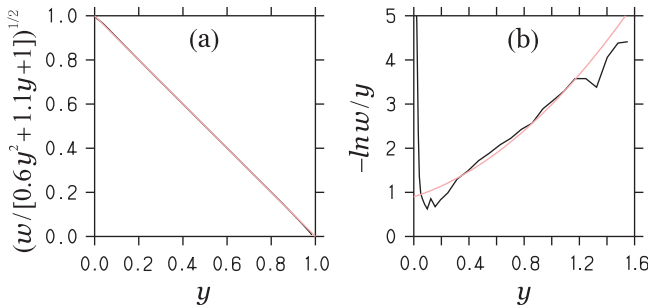
Figure A.4. Equations (A.18), (A.19) support: Figure (a) shows $(w/[0.6y^2 + 1.1y + 1])^{1/2}$ obtained from channel flow DNS data [64, 65] for $Re_\tau = 5186$ (black line). The pink line shows $1-y$. Figure (b) shows $-\ln w/y$ obtained from Pitot experimental data [72] for $Re_\tau = 65129$ (black line). The pink line shows $y(0.9 + y + 1.09y^2)$.

The U_1^+ curve is shown in Fig. A.1a in comparison to U^+. The asymptotic limit $U_{1\infty}^+$ of U_1^+ for $y^+ \to \infty$ can be obtained from Eq. (A.3) as

$$U_{1\infty}^+ = \frac{ac}{b}\left[B_1\left(\frac{c}{b}, -\frac{c}{b}\right) - B_1\left(c + \frac{c}{b}, -\frac{c}{b}\right)\right], \tag{A.9}$$

where $B_1()$ refers to the beta function. By using the definition of the beta function we see that the first term in the bracket is equal to zero. The second bracket term can be rewritten using the identity $BB_1(A, B) = (A + B)B_1(A, B + 1)$. The result reads $U_{1\infty}^+ = acB_1\left(c + \frac{c}{b}, 1 - \frac{c}{b}\right) = 15.85$. In the

following, U_1^+ will be referred to as wall damping contribution, which contributes to U^+ in addition to the logarithmic and wake contributions discussed below.

The difference $U^+ - U_1^+$, which is referred to as U_2^+ as long as wake effects (which will be added in Appendix A.3) are neglected, is shown in Fig. A.1d. We see that

$$U_2^+ = \frac{1}{\kappa} ln \left(1 + \frac{y^+}{y_\kappa} H \right) \tag{A.10}$$

combined with

$$H = \left[\frac{(y^+/h_1)^{h_2}}{1 + (y^+/h_1)^{h_2}} \right]^{h_3} \tag{A.11}$$

represents a very good model for $U^+ - U_1^+$ except in the wake region. The model parameters applied here are given by $\kappa = 0.4$, $y_\kappa = 75.8$, $h_1 = 12.36$, $h_2 = 1$, and $h_3 = 6.47$. The shear rate $S_2^+ = \partial U_2^+/\partial y^+$ implied by Eq. (A.10), which will be involved in discussions in the Supplementary Material, is given via the relation

$$\kappa y^+ S_2^+ = \frac{1 + h_3/[1 + y^+/h_1]}{1 + y_\kappa/(y^+ H)}. \tag{A.12}$$

The structure of Eq. (A.10) was found as follows. The function H is a transition function that varies between zero and one for very small and large y^+, respectively, see Fig. A.1d. Thus, Eq. (A.10) varies between zero (for $H = 0$) and $U_2^+ = ln(y^+/y_\kappa)/\kappa$. The latter asymptotic logarithmic variation of U_2^+ is supported by Fig. A.1d. However, the use of Eq. (A.10) in conjunction with $H = 1$ would lead to an inaccurate transition of U_2^+ from zero to its asymptotic logarithmic behavior, which provides motivation for the involvement of H: depending on three model parameters, the consideration of H enables the accurate reflection of changes of U_2^+ between zero and its asymptotic behavior. The structure of H follows the structure of $\langle u'v'\rangle_1^+$. Evidence for the suitability of the structure of H is provided in terms of the inset in Fig. A.1d. Equation (A.10) claims that the structure of H enables $ln(1 + y^+ H/y_\kappa)$ to represent the initial development of $\kappa(U^+ - U_1^+)$. In correspondence to Fig. A.1c, the inset in Fig. A.1d provides evidence for this claim.

The model parameters involved in Eq. (A.10) were determined in two steps. First, κ and y_κ were obtained by an analysis of the asymptotic logarithmic stage of U_2^+. In particular, κ and y_κ were obtained by considering the $U^+ - U_1^+$ DNS data points at about $y^+ = 500$ and $y^+ = 600$. The latter two values cover the core of the κ plateau region, see Fig. 3a. Second, the model parameters h_1, h_2, and h_3 were fixed by the requirement that the model Eq. (A.10) agrees exactly with the $U^+ - U_1^+$ DNS data at three points. This parameter calculation can be performed by finding h_3 analytically and varying h_1 and h_2 until the model values at two points agree with the known DNS data values.

In particular, with respect to $\kappa = 0.4$ obtained here for the von Kármán constant it is worth noting that this finding is obtained as an exact consequence of DNS data in the range $500 \leq y^+ \leq 600$ by excluding the wall damping contribution U_1^+. This approach is different to the approach discussed in Sect. 2.2 to determine κ.

A.2   Model Development II: Friction Law

To prepare the modeling of the velocity wake contribution in Appendix A.3, let us consider the validity of the friction law $U_\infty^+ = \kappa^{-1}(ln\, Re_\tau + C)$ for the three flows considered and derive its parameters from the observations applied here.

Figures A.2a-c support $U_\infty^+ = \kappa^{-1}(ln\, Re_\tau + C)$ combined with $\kappa = 0.4$ and a constant $C = (2.076, 2.382, 3.261)$ for channel, pipe, and TBL flow, respectively. Justification for these parameter settings was obtained in the following way. For channel flow, the DNS data of Lee & Moser [64, 65] and experimental data of Schultz & Flack [69] provide $\kappa = 0.4003$ and $\kappa = 0.3984$ least-squares estimates for κ, respectively. $C = 2.076$ provides then the best fit to DNS data. For the TBL, the DNS data [67, 68]) cover an insufficient range of Re_τ variations. The Pitot and NSTAP experimental data of Vallikivi et al. [72]) provide $\kappa = 0.3947$ and $\kappa = 0.3946$ least-squares estimates for κ, respectively.

$C = 3.261$ provides then the best fit to Pitot experimental data. For pipe flow, the DNS data of Chin et al. [66] and experimental data of Hultmark et al. [70, 71] provide $\kappa = 0.3968$ and $\kappa = 0.4134$ least-squares estimates for κ, respectively. So only in this case, there is a minor difference of κ values derived from DNS and experiments. The DNS value $\kappa = 0.4$ was applied in this case in conjunction with the conclusion of [27] that $\kappa = 0.40$ represents the most reliable κ value based on experimental pipe flow results. $C = 2.382$ provides then the best fit to DNS data.

For channel and pipe flow, the comparison with the corresponding model curves does not indicate any systematic deviation from $U_\infty^+ \propto ln\, Re_\tau$. It is surprising to observe relatively large, apparently random deviations of some DNS from $U_\infty^+ \propto ln\, Re_\tau$. With respect to channel (pipe) flow we observe that the DNS data of Lee & Moser [64, 65] (DNS data of Chin et al. [66]) are more consistently in agreement with $U_\infty^+ \propto ln\, Re_\tau$ than the DNS data of Lozano-Durán & Jiménez [73, 74] (DNS data of Ahn et al. [75]).

With respect to the TBL there is a very good agreement between the DNS data of Sillero et al. [67, 68] and experimental data for $Re_\tau \geq 1500$, whereas there are significant and systematic deviations between the DNS data of Sillero et al. [67, 68] and experiments for lower Re_τ. The reason for the latter deviations, which are also seen by using the DNS data of Schlatter & Örlü [76, 77], is a lack of recovery of the largest flow scales after an artificial inflow [67]: see also the discussion in Inoue & Pullin [98]. In particular, Sillero et al. [67] concluded that $Re_\theta \geq 4800$ is needed for the recovery of the largest flow scales after an artificial inflow. Figure A.2d shows the $Re_\theta - Re_\tau$ relationship based on the experimental Pitot and NSTAP data. It may be seen that $Re_\theta = 3.2 Re_\tau$ represents a very good approximation to the experimental data. Hence, $Re_\theta = 4800$ is equivalent to $Re_\tau = 1500$, which means that the requirement $Re_\tau \geq 1500$ seen here corresponds to the requirement $Re_\theta \geq 4800$ reported by Sillero et al. [67]. For completeness, the inset in Fig. A.2d shows the same for $Re_{\delta*}$ (which is often used for TBL analyses [31–36]) compared to the excellent approximation $Re_{\delta*} = 5 Re_\tau^{0.98}$. Both Pitot and NSTAP experimental TBL data [72] agree extremely well with the model. It has to be noted that the experimental data applied here made use of a skin friction relationship [99], which was found to be in very good agreement with other observations [72].

Overall and in agreement with previous conclusions [100, 101], the applicability of the same Reynolds number scaling with the same slope expressed by $U_\infty^+ = \kappa^{-1} (ln\, Re_\tau + C)$ reveals a remarkable similarity of the structure of the three flows considered. It is worth noting that [36] recently came to a slightly different conclusion. He applied $\kappa = 0.384$ regarding the logarithmic velocity variation in inner scaling for the three flows considered. With respect to κ based on the friction law, he applied $\kappa = (0.413, 0.420, 0.392)$ for channel flow, pipe flow, and the TBL, respectively. Here, the TBL κ value results from taking advantage of $Re_{\delta*} = 5 Re_\tau^{0.98}$. In contrast to the approach applied here, the channel flow and pipe flow κ were derived from four DNS data sets [64, 73, 102, 103] and earlier Princeton superpipe experimental data [83, 104]. A discussion of consequences of these κ value settings can be found in Sect. 3.4. We also note that $U_\infty^+ = \kappa^{-1} (ln\, Re_\tau + C)$ determines the skin friction coefficient via $c_f = 2/U_\infty^{+2}$ and the Reynolds number $Re_\infty = Re_\tau U_\infty^+$ based on the normalized centerline/freestream velocity U_∞^+.

A.3   Model Development III: Wake Layer

Figure A.1d shows that U^+ is well represented by $U_1^+ + U_2^+$, but there is a little deviation in the wake region, i.e., for relatively high y^+ values. This deviation $U_3^+ = U^+ - U_1^+ - U_2^+$, which accounts for wake effects, will be determined in this Appendix A.3 for the three flows considered. In particular, we will provide evidence for the suitability of $U^+ = U_1^+ + \kappa^{-1} ln \left([1 + Hy^+/y_\kappa]/[w + W_0] \right)$. In this way, the wake contribution $U_3^+ = -\kappa^{-1} ln\, (w + W_0)$ to the mean velocity is provided via w and W_0. The functions w and W_0 will be derived below depending on the Reynolds number and flow considered.

Let us obtain first insight into the structure of U_3^+. Figure A.1d shows that U_3^+ is nonzero in the asymptotic regime (for relatively high y^+ values). Thus, to determine U_3^+ we can use the relation

$$\left(U^+\right)_{as} = U_{1\infty}^+ + U_{2\infty}^+ + U_3^+. \tag{A.13}$$

Here, the subscript *as* refers to the asymptotic limit of U^+. We know $U_{1\infty}^+ = 15.85$ according to Eq. (A.8) and $U_{2\infty}^+ = \kappa^{-1}ln(y^+/y_\kappa)$ according to Eq. (A.10). In particular, $(U^+)_{as}$ differs from $U^+ = U_1^+ + U_2^+ + U_3^+$ by the consideration of asymptotic limits of U_1^+ and U_2^+ in Eq. (A.13). Figure A.1d shows that the asymptotic $(U^+)_{as}$ can be considered as a slightly modified version of $U_{1\infty}^+ + U_{2\infty}^+$. Correspondingly, we consider the following modified version of Eq. (A.13),

$$(U^+)_{as} = U_{1\infty}^+ + \kappa^{-1}ln\left(\frac{y^+}{y_\kappa W}\right), \tag{A.14}$$

which is equivalent to introducing U_3^+ as $U_3^+ = -\kappa^{-1}ln\,W$. By making use of $U_3^+ = -\kappa^{-1}ln\,W$, the complete velocity $U^+ = U_1^+ + U_2^+ + U_3^+$ is given by

$$U^+ = U_1^+ + \kappa^{-1}ln\left(\frac{1 + y^+ H/y_\kappa}{W}\right). \tag{A.15}$$

Here, the wake function W, which refers to the wake effect, is given according to Eq. (A.14) by

$$W = e^{-\kappa[(U^+)_{as} - U_{1\infty}^+]}\frac{y^+}{y_\kappa}. \tag{A.16}$$

Next, let us specify the structure of W. The advantage of the approach applied is its ability to reflect the most important feature of the mean velocity in the asymptotic stage, the leveling off of the mean velocity, in the simplest possible way. To show this we consider Eq. (A.16) in the asymptotic y^+ regime,

$$W_0 = e^{-\kappa(U_\infty^+ - U_{1\infty}^+)}\frac{y^+}{y_\kappa}. \tag{A.17}$$

Here, W_0 is the asymptotic wake function, and U_∞^+ is the constant centerline/freestream velocity. The constant U_∞^+ can be parametrized by the friction law Eq. (3), $U_\infty^+ = \kappa^{-1}(ln\,Re_\tau + C)$, which is implied by the log-law [2, 27, 80]. It is worth noting that this equation does not involve any assumption as long as C is not defined. To account for deviations from W_0, the wake function W will be considered to consist of two contributions, $W = W_0 + w$, where w, which is given by the difference of Eqs. (A.16) and (A.17), refers to deviations from W_0. The remaining tasks are (i) to provide evidence for the suitability of Eq. (3) by showing that $U_\infty^+ \propto ln\,Re_\tau$ and C is a constant, and (ii) to determine the deviation w from the asymptotic wake behavior. The first problem was already solved in Appendix A.2. The second problem will be solved in the next two paragraphs.

Figures A.3a-c show w for channel, pipe, and TBL flow obtained by using the DNS data of Lee & Moser [64, 65], DNS data of Chin et al. [66], and Pitot experimental data of Vallikivi et al. [72], respectively. With respect to this calculation of w, the individual U_∞^+ data given by the corresponding DNS and experimental data were applied. The DNS data of Lee & Moser [64, 65] and DNS data of Chin et al. [66] were applied because of their better agreement with $U_\infty^+ \propto ln\,Re_\tau$. Given the significant deviations of lower Re_τ DNS data of Sillero et al. [67, 68]) from $U_\infty^+ \propto ln\,Re_\tau$ and the excellent agreement of experimental data with $U_\infty^+ \propto ln\,Re_\tau$, the experimental data were applied to calculate w for the TBL. In particular, the Pitot experimental DNS data were used. The reason for that is explained in terms of Fig. A.3d, which shows Pitot and NSTAP calculations of w for $Re_\tau = 65129$ and $Re_\tau = 72526$, respectively. For small y, w needs to approach one such that $W = W_0 + w$ affects the mean streamwise velocity only in the asymptotic y^+ regime, see Eq. (A.15) and the discussion in the beginning of this Appendix A.3. Although the NSTAP experimental data are in agreement with $W(0) = w(0) = 1$, the Pitot experimental data show a smoother transition to $W(0) = w(0) = 1$ in the region of small y values.

The most significant result of calculating w from DNS and experimental data is that there is no significant Re_τ effect on w. With respect to both channel and pipe flow, it was found that $w = w_{CP}$, where

$$w_{CP} = 0.1(1 - y)^2\left[6y^2 + 11y + 10\right], \tag{A.18}$$

represents an excellent model for these DNS estimates (the subscript *CP* refers to channel and pipe flow): see Figs. A.3a-b. In agreement with the features seen in Figs. A.2a-b, it appears that the channel

flow DNS data collapse slightly better than the corresponding pipe flow results. Eq. (A.18) was found by using a fourth-order polynomial in conjunction with the constraint to pass exactly through 5 data points given by the $Re_\tau = 5186$ channel flow curve. With respect to the TBL, we see that $w = w_{BL}$, where

$$w_{BL} = e^{-y(0.9+y+1.09y^2)}, \tag{A.19}$$

represents the experimental data very well (the subscript BL refers to boundary layer flow): see Fig. A.3c. Given the possibility to use the same w for both channel and pipe flow, it is interesting to see that w for the TBL is described by an exponential function and not a polynomial. The reason for the need to use different w structures is given by the bounded channel and pipe flow, and the unbounded TBL (see also the discussion in Sect. 3.3). The latter is reflected by $w = 0$ at $y = 1$ for channel and pipe flow, and the lack of $w = 0$ for finite y for the TBL. The suitability of structures applied to model w_{CP} and w_{BL} is confirmed in terms of Fig. A.4, which shows w_{CP} and w_{BL} by following in part the structure of Eqs. (A.18)-(A.19). The comparison with the corresponding linearities involved in Eqs. (A.18)-(A.19) clearly demonstrates the suitability of polynomials and exponential functions applied. In particular, Fig. A.4b was used to find the model Eq. (A.19).

The shear rate $S_3^+ = \partial U_3^+/\partial y^+$ related to U_3^+ matters regarding the discussions in the Supplementary Material. By using the expressions derived above we obtain

$$\kappa y^+ S_3^+ = -\frac{1 + w'y/W_0}{1 + w/W_0} = -\frac{1 + w'/K}{1 + w/(Ky)}. \tag{A.20}$$

Here, w' refers to the derivative of $w(y)$, which is given by

$$w'_{CP} = \left(\frac{12y+11}{6y^2+11y+10} - \frac{2}{1-y}\right)w_{CP}, \qquad w'_{BL} = -(0.9 + 2y + 3.27y^2)w_{BL}. \tag{A.21}$$

The last expression in Eq. (A.20) involves $K = y_\kappa^{-1}e^{\kappa U_{1\infty}^+ - C}$, which is a flow-dependent constant. By using Eqs. (A.20) and (A.21), $\kappa y^+ S_3^+$ for channel/pipe flow and the TBL can be written

$$\left(\kappa y^+ S_3^+\right)_{CP} = (1-y)G_{CP} - 1, \qquad \left(\kappa y^+ S_3^+\right)_{BL} = G_{BL} - 1, \tag{A.22}$$

where

$$G_{CP} = \frac{1 + y + y^2(1.6 + 1.8y)}{Ky + (1-y)^2(0.6y^2 + 1.1y + 1)}, \qquad G_{BL} = \frac{1 + (0.9 + 2y + 3.27y^2)y}{1 + Kye^{y(0.9+y+1.09y^2)}}. \tag{A.23}$$

G_{CP} is a function that varies between 1 and $5.4/K$, and G_{BL} varies between 1 and 0.

Appendix B. Model Validation

The velocity model derived in Appendix A is validated here by DNS and experimental data.

### B.1 Comparison with DNS and Experiments: Moderate Re_τ

Comparisons of the PVM with DNS and experimental data are shown in Figs. B.1, B.2, B.3. First, let us consider these comparisons for $500 \leq Re_\tau \leq 2000$. With respect to the TBL, only DNS data are involved which do not suffer from an insufficient development of large scales, see the discussion in Appendix A.2. The TBL model curves are plotted up to $y = e^3$. Model errors e_M and data errors e_D in percent (the maximum of the values at all available data points) are presented in Table B1. The model errors e_M result from the relative model errors. For DNS, the relative error of the DNS U_∞^+ compared to Eq. (3) is used as a measure to indicate the DNS data error e_D. For experimental data, we use the relative error e_D of experimental data at about $y^+ = 5$ with respect to the corresponding U_1^+ value: it was shown above that U_1^+, which is strongly supported by DNS data, is valid up to at least $y^+ = 10$, see Fig. A.1a. These definitions of data errors may be considered to indicate global errors. With respect to DNS, the error related to the momentum balance increases with the distance from the wall (see reference [44]). With respect to experiments, the error due to the imprecision in
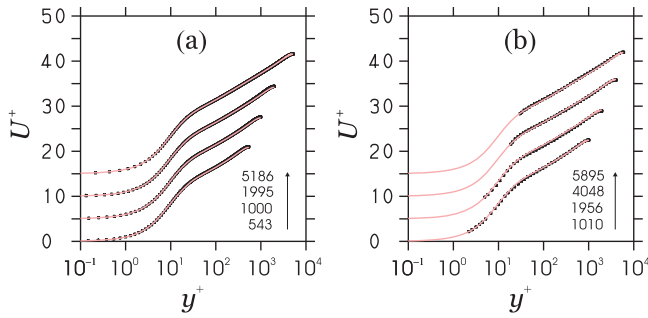
Figure B.1. Channel flow: The PVM (pink lines) is compared in (a) to DNS data of Lee & Moser [64, 65] and (b) experimental data of Schultz & Flack [69] (black dots) for the given Re_τ (separated by $\triangle U^+ = 5$).
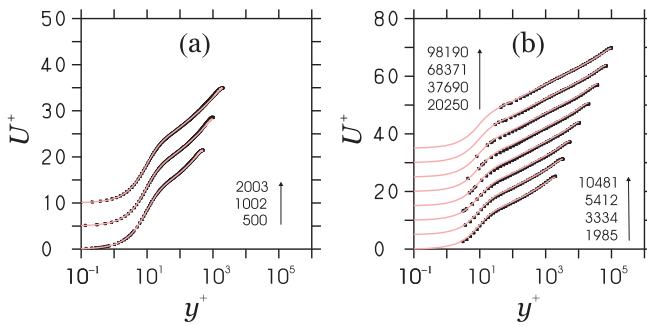
Figure B.2. Pipe flow: The PVM (pink lines) is compared in (a) to DNS data of Chin et al. [66] and (b) experimental data of Hultmark et al. [70, 71] (black dots) for the given Re_τ (separated by $\triangle U^+ = 5$).
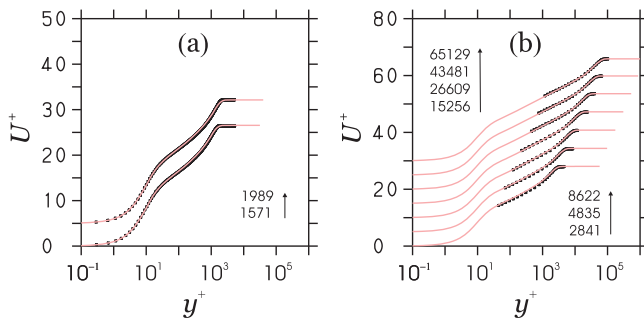

Figure B.3. TBL: The PVM (pink lines) is compared in (a) to DNS data of Sillero et al. [67, 68] and (b) Pitot experimental data of Vallikivi et al. [72]) (black dots) for the given Re_τ (separated by $\triangle U^+ = 5$).

the measurement of the wall distance decreases with the wall distance (see also the discussion at the end of Appendix A.1 related to Fig. B.4).

Overall, the comparison of the PVM with DNS and experiments reveals an impressive model performance. Compared to DNS, the model errors e_M are below 1.7% for all three flows considered. We see that e_M compares very well with e_D (the TBL e_D arises from only two data points $Re_\tau = (1571, 1989)$; due to the scatter of data it may be expected that this e_D is slightly underpredicted). It

Table B1. Model errors e_M and data errors e_D in percent. E-PP and E-LL refer to experiments providing partial profile (PP) and log-law (LL) support, respectively.

DNS & Experiments		Channel		Pipe		TBL	
		e_M	e_D	e_M	e_D	e_M	e_D
a) $500 \leq Re_\tau \leq 2000$:	DNS	0.9	0.9	1.7	1.4	1.3	0.4
	E-PP	4.4	2.4	18	18	—	—
b) $2000 < Re_\tau \leq 10^5$:	DNS ($Re_\tau = 5200$)	0.3	0.0	—	—	—	—
	E-PP ($Re_\tau \leq 4 \times 10^4$)	—	—	9.0	9.0	—	—
	E-LL (all Re_τ range)	1.5	—	3.5	—	2.8	—
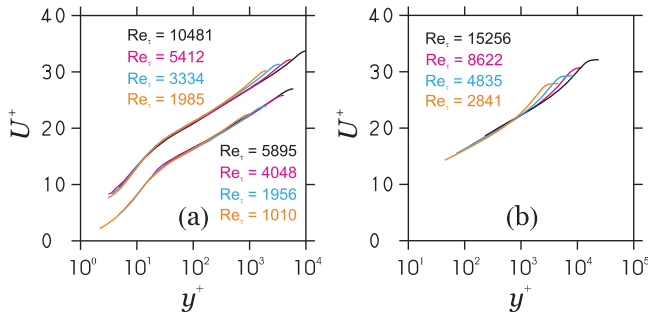
Figure B.4. Experimental data for the given Re_τ: (a) channel flow data of Schultz & Flack [69] and pipe flow data of Hultmark et al. [70, 71]; (b) TBL data of Vallikivi et al. [72]. The pipe flow data in (a) are moved up by $+5$.

is worth noting that it is impossible for e_M to be smaller than e_D. This comparison seems to indicate that the main reason for the e_M model error is given by the scatter of DNS data.

The comparison of the velocity model with experimental results shows a larger model error than seen in comparison to DNS. However, it is relevant to note that this model error is, basically, implied by the corresponding scatter of data (again, e_M cannot be smaller than e_D). Figure B8 supports this view by showing only experimental data for the lowest four Reynolds numbers. It may be seen, for example, that the experimental velocity profiles in the viscous region clearly show that the experimental data are affected by noise. With respect to pipe flow, we find $e_M = e_D$. For channel flow we find that e_M is slightly larger than e_D, but this finding seems to be affected by the fact that the channel e_D was obtained from only two data points, $Re_\tau = (1010, 1956)$. It is worth noting that support for the velocity model via experiments is not only provided for the log-law region, but the complete velocity profile is at least partially included.

B.2   Comparison with DNS and Experiments: High Re_τ

The comparisons presented in Appendix A.1 do not give clear answers to two questions: (i) how can we quantify the model error without considering cases of (significant) data errors (in conjunction with the fact that e_M cannot be smaller than e_D), and (ii) which support has the velocity model for higher Reynolds numbers. These questions can be addressed by considering comparisons with DNS and experiments for $2000 < Re_\tau \leq 10^5$. The corresponding errors are shown in Table B1.

DNS data with an almost zero e_D are available for $Re_\tau = 5200$. Remarkably, the corresponding model error e_M is only 0.3%. The calculation of e_D as described above is only one possibility to define a data error. Another way would be to look at the relative error of satisfying the momentum equation $S^+ - \langle u'v' \rangle^+ = 1 - y$. This data error is 0.23% for the case considered, which is comparable to $e_M = 0.3\%$. Therefore, we can conclude that the PVM is extremely accurate and only limited by the error of DNS (as it has to be expected according to the model development).

The comparison with corresponding experimental data provides strong support for the application of the model at higher Reynolds numbers. With respect to this question, it is helpful to differentiate between experimental results that provide support for more than the log-law region (E-PP, partial profile support), and experimental results that provide only support in the log-law region (E-LL, log-law support). The comparison of the model with E-LL leads to the conclusion that the model performance is excellent. The corresponding models errors e_M are below 3.5% for all three flows considered, see Table B1. The largest value $e_M = 3.5\%$ was obtained for pipe flow based on only two data points $Re_\tau = (68371, 98190)$. The comparison of the model with E-LL is only possible with respect to pipe flow: we have $e_M = e_D = 9.0\%$. However, this relatively large model error is simply a consequence of the data error: the model error cannot be smaller than the data error. The more important fact of both model comparisons with E-LL and E-PP is that these comparisons clearly demonstrate the applicability of the PVM for high Reynolds number flows.